J Sol-Gel Sci Technol (2017) 84:206–213
DOI 10.1007/s10971-017-4488-7

ORIGINAL PAPER: SOL-GEL AND HYBRID MATERIALS FOR OPTICAL, PHOTONIC AND OPTOELECTRONIC APPLICATIONS

Structural, morphological and optical properties of SnO_2 nanoparticles obtained by a proteic sol–gel method and their application in dye-sensitized solar cells

M. S. Pereira[1] · F. A. S. Lima[1,3] · C. B. Silva[2] · P. T. C. Freire[2] · I. F. Vasconcelos[1]

Received: 5 June 2017 / Accepted: 31 July 2017 / Published online: 22 August 2017

Abstract Tin dioxide nanoparticles were synthesized by the proteic sol–gel method. Tin chloride ($SnCl_4{\cdot}5H_2O$) was used as source of Sn_{4+} and commercial gelatin as organic precursor. Several calcination temperatures were employed. Thermogravimetric analysis and differential scanning calorimetry were performed to investigate the thermal behavior of the precursor powders as well as to select the appropriate calcination temperatures for oxide formation. Structural, morphological, and optical properties of the synthesized materials were studied by X-ray diffraction, transmission electron microscopy, Fourier transformed infrared spectroscopy, and ultraviolet–visible spectroscopy. The results confirmed the formation of spherical nanoparticles of rutile SnO_2 with an optical absorption band in the ultraviolet region near the visible light range. Thermally treated samples showed improved crystallinity and superior transparency to visible light. These SnO_2 nanoparticles were successfully employed as photoanode material in dye-sensitized solar cells. The performance of the cells was evaluated by measuring $J \times V$ curves in a solar simulator and was found to be in line with results in the literature.

Graphical abstract

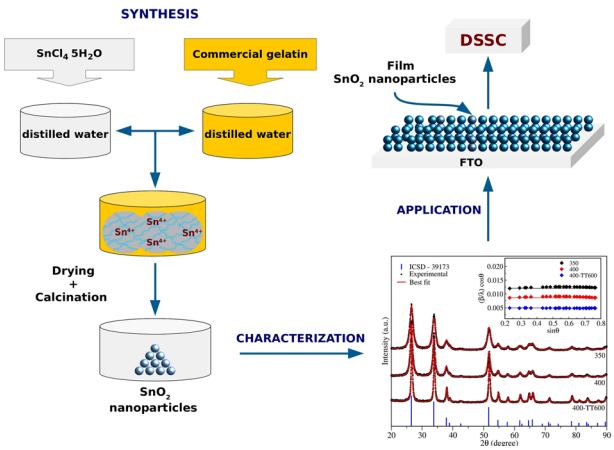

Keywords SnO_2 nanoparticles · Proteic sol–gel method · Dye-sensitized solar cells · Emerging technologies

1 Introduction

Tin dioxide (SnO_2) is a typical wide band gap n-type semiconductor with direct band gap of about 3.6 eV at room temperature. It is one of the most widely used semiconductor oxide due to its chemical and mechanical stability [1] and excellent optical and electrical properties [2, 3]. It has a rutile-type tetragonal crystal structure with a $P4_2/mnm$ space group [4, 5]. Its unit cell consists of two Sn^{4+} and four O^{2-} ions with each tin cation coordinated by six oxygen anions in the corners of a regular octahedron. Each oxygen anion is surrounded by three Sn^{4+} ions which

✉ M. S. Pereira
mauriciosousa@alu.ufc.br

[1] Department of Metallurgical and Materials Engineering, Universidade Federal do Ceará, Fortaleza, Brazil

[2] Department of Physics, Universidade Federal do Ceará, Fortaleza, Brazil

[3] Present address: Organic Electronics Division, CSEM Brasil, Belo Horizonte, Brazil

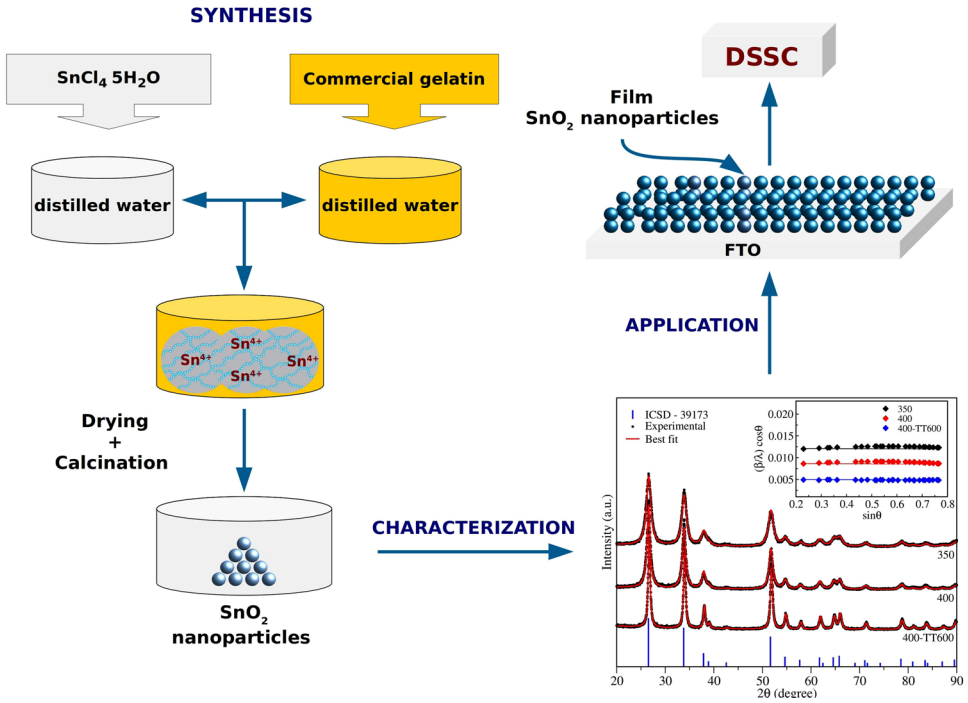

Fig. 1 Schematic representation of nanoparticles synthesis and DSSC building

approximate the corners of an equilateral triangle [5]. Tin oxide has many technological applications such as in solar cells [6–8], photocatalytical activity [9], gas sensors of toxic materials [10, 11], liquid crystal displays and anodes for lithium ion batteries [12].

The synthesis of SnO_2 nanoparticles has been carried out by different methods such as solid-state reaction methods [13], chemical precipitation [14, 15], and conventional sol–gel [16, 17], among others. Sol–gel methods present several advantages over other methods such as a potential to produce high purity compounds with homogeneity at the atomic scale, as well as a significant reduction of required processing times and temperatures.

The proteic sol–gel [18] method used in this work is a variation of the conventional method that employs edible gelatin or coconut water as organic precursor for oxide formation. This method has been successfully employed in the synthesis of nanometric semiconducting materials with potential use in various technological applications [19–21]. As it uses low cost reagents like metal nitrates and chlorides, this method is relatively simple and cost efficient.

The synthesis by the proteic sol–gel method consists of four stages: dissociation of metal ions from precursor salts, formation of metal-gelatin chelates, drying, and calcination. In the first stage metal ions are dissociated from the precursor salts in distilled water. The solution with dissociated ions is put in contact with the gelatin to form metal chelates where metal ions join the functional groups (amino acids) of the gelatin. The drying stage is employed to remove water and form a puffy polymeric substance. Finally, calcination is performed to remove organic matter with formation of the desired compound. When calcination is done in open air, oxides of the metallic ions are formed. Calcination temperatures are generally just low enough to evaporate the organic matter without affecting the outcome of the reaction.

This work presents structural, morphological, and optical characterization of SnO_2 nanoparticles produced by the proteic sol–gel method. The material was applied as photoanode in dye-sensitized solar cells (DSSC) to demonstrate its technological viability.

2 Experimental procedure

The entire process of nanoparticles synthesis and DSSC building is schematically represented in Fig. 1 and described below.

2.1 Nanoparticles synthesis and characterization

Samples of nanoparticulated SnO_2 were prepared by the proteic sol–gel method [18]. $SnCl_4 \cdot 5H_2O$ was employed as source of Sn^{4+} ions and commercial gelatin as organic precursor. In a typical procedure, two separate solutions were produced by dissolving 10 g of $SnCl_4 \cdot 5H_2O$ and 5 g of commercial gelatin in 10 and 20 mL, respectively, of distilled water, and stirred for 60 min in room temperature. Both solutions were added together under continuous stirring at temperature of 40 °C for 10 h to promote

polyesterification. This mixture was then dried at 150 °C in air during 24 h to remove volatile components, resulting in a black solid puffy mass, referred to in this text as the precursor powder.

The precursor powder was calcined at 350 and 400 °C (at a heating rate of 5 °C/min) in air atmosphere for 4 h, resulting in the SnO_2 nanoparticles. The sample calcined at 400 °C was submitted to a thermal treatment at 600 °C in air atmosphere for 2 h in order to eliminate residual organic matter. These samples are referred to throughout this paper as 350, 400, and 400–TT600, respectively.

Thermogravimetric analysis (TGA) and differential scanning calorimetry (DSC) were performed using a NETZSCH STA 449F3 Jupiter thermal analysis equipment. Measurements were performed under air atmosphere with heating hate of 5 °C/min.

X-ray diffraction (XRD) patterns were collected at room temperature using a Rigaku DMAXB diffractometer operating with a Kα-Cu source ($\lambda = 1.54$ Å) at 40 kV and 30 mA. The pattens were Rietveld refined [22, 23] using the program GSAS [24] and based in the SnO_2 standard crystal structure cataloged by the Inorganic Crystal Structure Database under number 39173 (ICSD-39173).

Transmission electron microscopy (TEM) were performed using a 200 kV JEM 2011 microscope. Fourier transformed infrared (FTIR) absorption spectra were collected at room temperature in transmission mode using a Bruker Vertex 70 spectrometer. Ultraviolet–visible (UV–Vis) spectroscopy was carried out at room temperature using a UV 2600 Shimadzu spectrophotometer coupled to an integrating sphere ISR 2600 Plus. Scanning electron microscopy (SEM) of photoanode films was performed in air under ambient conditions using a Quanta FEG 450 microscope.

2.2 Solar cells construction and characterization

400-TT600 nanoparticles were used as photoanode in the production of DSSC. An amount of 250 mg of SnO_2 nanoparticles were dispersed in a mixture of ethanol (0.5 mL), Triton-X-100 (two drops), acetic acid (0.02 mL) and isopropanol (0.25 mL). The solution was placed in an ultrasonic bath for 1 h, and subsequently kept under stirring at room temperature for 24 h. A SnO_2 photoanode was prepared using the spin coating method with the prepared semiconductor solution applied on a FTO substrate. The photoanode was then sintered at 450 °C for 30 min. The SnO_2 electrodes prepared as described above were dipped into a solution of N719 dye in acetonitril for 24 h at room temperature and then rinsed with ethanol and dried under a nitrogen gas flow. The dye-adsorbed SnO_2 electrode and Pt-counter electrode were assembled into a sandwich-type cell and sealed with a hot-melt film. The electrolyte (Iodolyte AN-50) was inserted through a hole that was sealed using the hot-melt film.

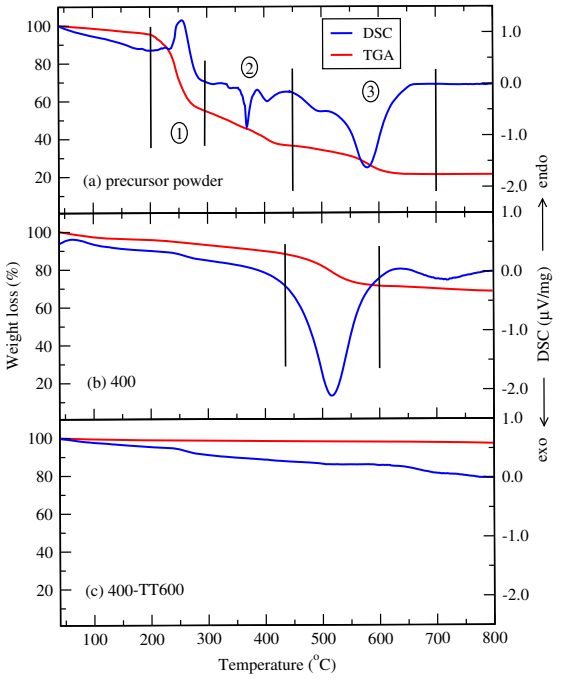

Fig. 2 TGA/DSC curves of **a** precursor powder, **b** sample 400 and **c** sample 400-TT600

Solar simulations were performed using a Steuernagel Solarkonstant KHS1200 solar simulator under simulated AM 1.5 solar illumination at 100 mW/cm^2. J × V curves were measured using a Keithley 2601 multimeter.

3 Results and discussion

Thermal analysis was performed in order to study the thermal decomposition of the materials and to select the appropriate temperatures of oxide formation and thermal treatment. Figure 2 shows TGA/DSC curves obtained from the precursor powder and SnO_2 samples calcined at 400 °C before and after thermal treatment.

The thermal behavior of the precursor powder may be divided into three main stages as indicated in Fig. 2a. The first one occurs in the 200–300 °C range and can be attributed to the thermal degradation of gelatin chains. This reaction is characterized by an endothermic peak at about 250 °C in the DSC scan and is responsible for the loss of about 40% of the sample mass. The second stage occurs between 300–450 °C where the sharp DSC exothermic peak at about 370 °C is attributed to the formation of SnO_2 [10, 25]. Some organic matter is decomposed in this stage as the

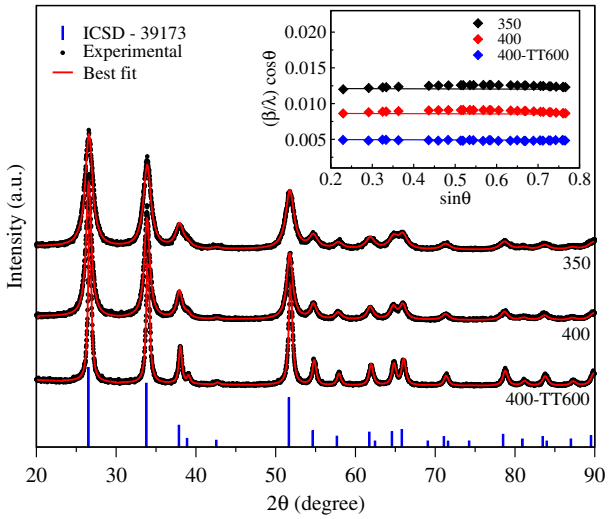

Fig. 3 X-ray diffraction patterns of SnO_2 samples 350, 400, and 400–TT600. *Dots* and *solid lines* are the experimental data and best fit respectively. *Bars* represent the ICSD-39173 standard pattern. Insert: Williamson–Hall curves

TGA curve shows an approximate loss of 20% of mass. The third and last stage takes place in the temperature range of 450–700 °C. The exothermic peak around 580 °C is due to carbonate decomposition releasing carbonyl groups [25–27]. Another 20% of mass is lost in this stage adding up to a total of 80% of mass loss in the entire process.

These results suggest that SnO_2 formation occurs at temperatures between 350 and 400 °C. The thermal analysis of a sample calcined at 400 °C for 4 h is showed in Fig. 2b. A single thermal event, responsible for a 15% moss loss, is observed in the 450–600 °C range. The broad exothermic peak at around 515 °C is attributed to the formation and evaporation of CO_2 [25–27]. This result indicates that the calcination process did not eliminate the organic matter entirely. This sample was then treated at 600 °C for 2 h and its thermal behavior is shown in Fig. 2c. The DSC shows no endo or exothermic processes and the TGA shows no mass loss, confirming that all organic matter has been eliminated by the thermal treatment.

Figure 3 shows XRD patterns of SnO_2 samples. All diffractograms show peaks that match the ICSD-39173 reference pattern relative to the tetragonal crystal structure of SnO_2 (bars in the figure). No other crystalline phase was found.

The patterns were Rietveld refined and the best fits are shown as solid red lines. Williamson–Hall curves [28] are shown in the inset of Fig. 3. Table 1 shows lattice parameter, unit cell volume, and crystallite average size as calculated by the Scherrer formula (D_S) and corrected by the Williamson–Hall method (D_{WH}) after compensating for residual microstrain (ε). Lattice parameters (and unit cell volume) values are virtually the same for all samples. All

Table 1 Lattice parameters, unit cell volume, average crystallite size, and microstrain of SnO_2 samples 350, 400, and 400-TT600

Sample	$a = b$ (Å)	c (Å)	Volume (Å^3)	D_S (nm)	D_{WH} (nm)	ε (%)
350	4.740	3.185	71.55	8.1	8.2	0.01
400	4.738	3.185	71.52	11.0	11.0	−0.01
400–TT600	4.743	3.189	71.75	20.6	20.3	−0.04

samples showed crystallite size in the nanometer range (8–20 nm) with negligible levels of microstrain. The thermal treatment led to an increase of particle size from 11 (sample 400) to about 20 nm (sample 400-TT600). Sample homogeneity improved with thermal treatment as the Williamson–Hall curve of the 400-TT600 sample is more akin to a straight line.

Figure 4 shows TEM images (two different magnifications) of a SnO_2 sample calcined at 350 °C. It can be seen that SnO_2 nanoparticles have an approximate spherical morphology with an average diameter between 5 and 10 nm, in agreement with the sizes obtained from the XRD data.

A zoomed-in image of a nanoparticle is shown on the inset of Fig. 4a. The selected area of electron diffraction pattern of the sample is shown on the inset of Fig. 4b. The interplanar distance shown in Fig. 4a was estimated as approximately 0.33 ± 0.02 nm, which corresponds to the {110} diffraction planes of the rutile-type structure. It is worth mentioning that these diffraction planes are commonly found in nanosized SnO_2 systems. These values are in agreement with those reported in the literature [9, 29]

FTIR spectra of the precursor powder and SnO_2 nanoparticles are shown in Fig. 5. The precursor powder spectrum exhibits absorption bands in a wide range attributed to gelatin. The absorption peak at 890 cm^{-1} is assigned to C–H bending modes in alkene groups [30]. The peaks at 1405 and 1478 cm^{-1} are attributed to C–O and N–H vibration bands, respectively [30–32]. The broad absorption region in the range 1360–1760 cm^{-1}, centered at 1572 cm^{-1}, is assigned to overlapping vibration modes of carboxylic, alkene and amine groups (C=O, C=C and N−H) present in gelatin [30–32, 34]. The peak appearing at around 1105 cm^{-1} is attributed to the vibration of the hydroxyl-tin (Sn–OH) bond [2, 33]. The broad absorption bands centered at 1740 and 3160 cm^{-1} are attributed, respectively, to bending and stretching vibrations of hydroxyl groups of water molecules.

FTIR spectra of SnO_2 nanoparticles show intense absorption bands at a lower wave number range of 465–610 cm^{-1} characteristics of Sn–O stretching modes expected for crystalline SnO_2 [34–37]. The spectrum for the 400–TT600 sample presents narrower band widths and

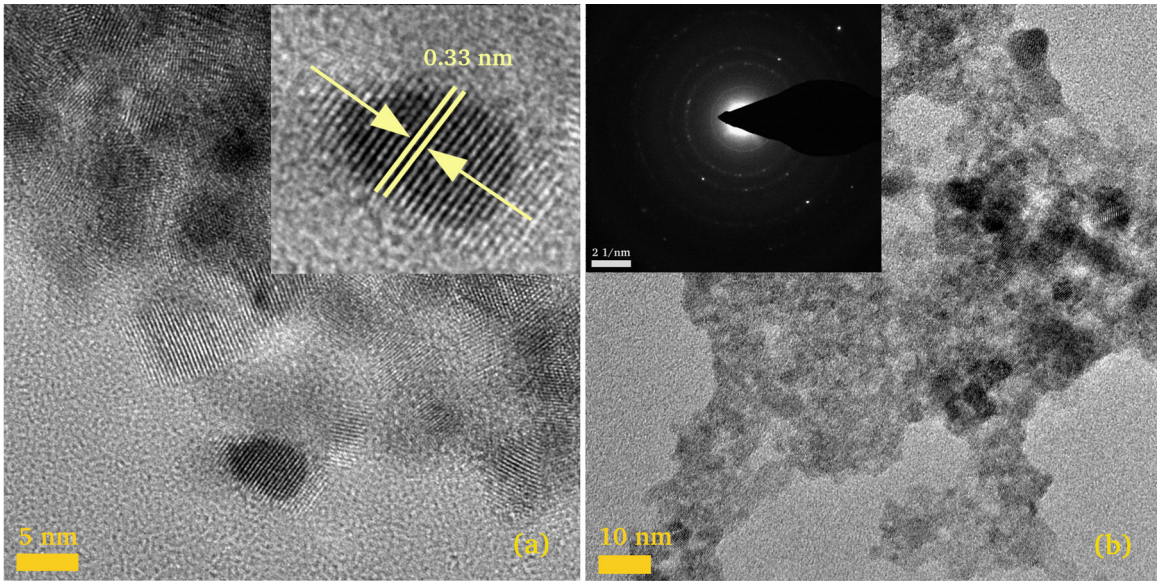

Fig. 4 TEM images (two different magnifications) of SnO_2 nanoparticles calcined at 350 °C. *Inset*: a zoomed-in image of a nanoparticle and corresponding selected area electron diffraction (SAED) pattern

larger intensities attributed to the improvement in crystallinity due to the removal of residual organic matter.

Samples 350 and 400 spectra present a region of overlapped broadened bands between 800 and 1750 cm^{-1} resulting from vibrations of functional groups present in the gelatin still remaining after calcination. These bands are absent from the spectrum of the 400–TT600 sample providing further confirmation that all residual organic matter has been eliminated by the thermal treatment. The 1740 and 3160 cm^{-1} bands attributed to water molecules are absent from all calcined samples spectra.

UV–Vis absorbance spectra of SnO_2 samples are shown in Fig. 6. The curves display an absorption band in the ultraviolet region near the visible light range. The samples 350 and 400 are translucent and exhibit a dark color due to the presence of residual organic material from the synthesis. As expected, the sample 400–TT600 showed superior transparency to visible light due to the absence of organic matter.

As the absorbance spectra of these nanoparticles do not show very sharp absorption edges, the point of inflection obtained from the maximum of the first derivative can be considered to represent the absorption edge [38]. Therefore, energy band gaps were estimated by taking the maximum of the first derivative of each absorbance spectrum (shown in the inset of Fig. 6). The band gap of samples 350 and 400 was estimated as 3.92 eV and of sample 400–TT600 as 3.85 eV. This slight narrowing of the band gap is due to improved crystallinity and increased crystallite size of 400–TT600 nanoparticles.

High transmittance in the visible and large electron mobility are two characteristics of a material that makes it

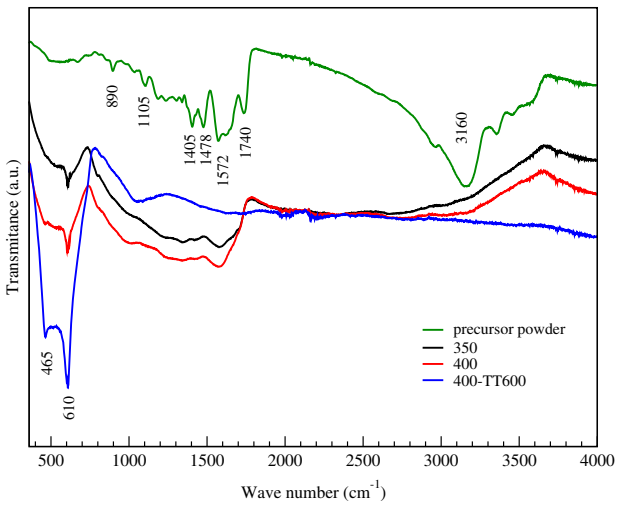

Fig. 5 FTIR spectra of the precursor powder and SnO_2 samples 350, 400, and 400–TT600

suitable to be used as photoanode in DSSCs. The results showed that the 400–TT600 nanoparticles have better crystallinity and are free of residual organic matter and thus are expected to have improved electron mobility when compared to the 350 and 400 nanoparticles. Moreover, UV–Vis results showed superior transparency of 400–TT600 nanoparticles in the visible region of the electromagnetic spectrum. Therefore, the 400–TT600 nanoparticles were chosen to be used as photoanode in the construction of DSSCs.

Figure 7 shows SEM images of a SnO_2 photoanode film after the dye-loading. Upon deposition, nanoparticles form micrometer-sized agglomerates as can be observed on the

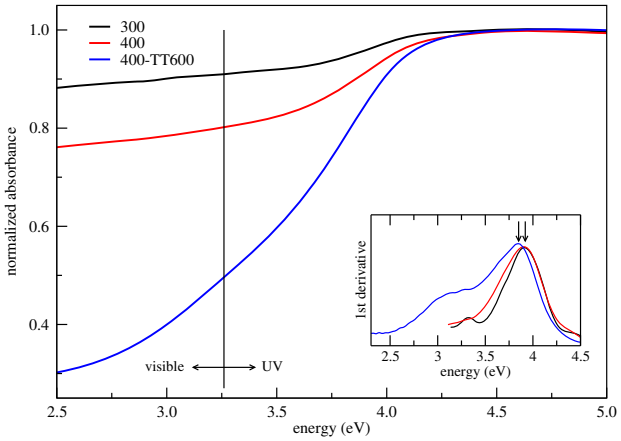

Fig. 6 UVV is absorbance spectra of SnO_2 samples 350, 400, and 400–TT600. *Inset*: first derivative with *arrows* identifying the points of maxima

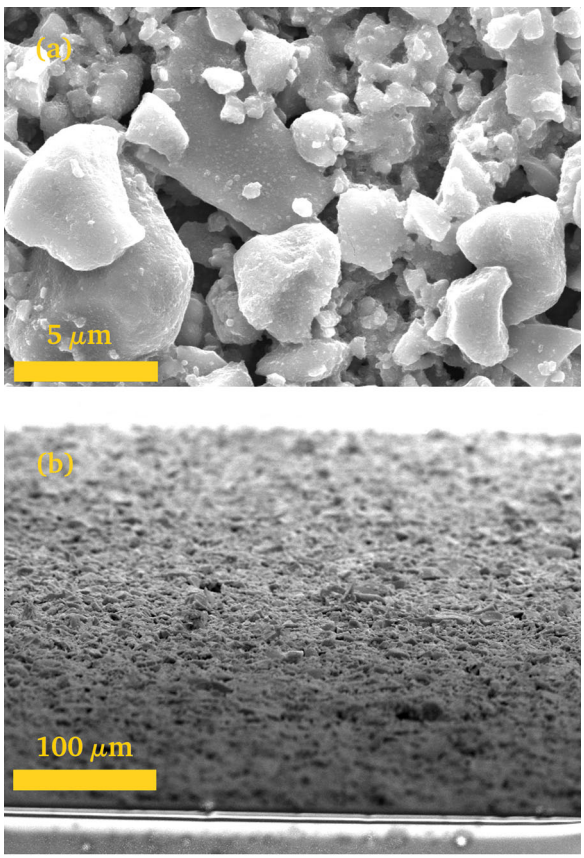

Fig. 7 SEM images of a SnO_2 photoanode film from: **a** *top view* and **b** cross sectional view after the dye-loading

top-view image showed in Fig. 7a. Film thickness was estimated from the cross-sectional-view image showed in Fig. 7b and was found to be larger than 100 µm. Voids in the film with a few micrometers can also be observed.

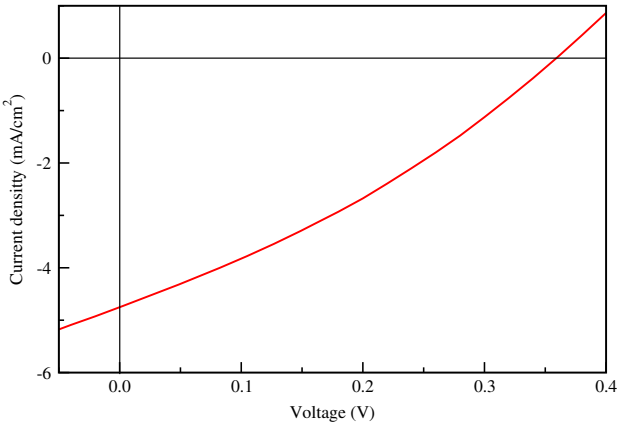

Fig. 8 $J \times V$ curve of the best DSSC using SnO_2 nanoparticles as photoanode. Under simulated AM 1.5 solar illumination at 100 mW/cm^2

Table 2 Photovoltaic parameters of DSSCs employing SnO_2 nanoparticles as photoanodes

Devices	J_{sc} (mA/cm^2)	V_{oc} (V)	FF (%)	η (%)	R_s (Ω cm^2)	R_{sh} (Ω cm^2)
D1	4.74	0.36	31.40	0.53	19	114
D2	3.42	0.40	33.67	0.45	63	313
D3	3.80	0.31	26.00	0.30	74	86
D4	3.54	0.30	29.00	0.30	41	116
D5	2.60	0.30	31.00	0.25	39	180
Avg	3.62 ± 0.33	0.34 ± 0.040	30.20 ± 2.88	0.36 ± 0.11	47 ± 24	162 ± 104

J_{sc}, V_{oc}, FF, η, R_s, and R_{sh} are short-circuit current density, open-circuit voltage, fill factor and power conversion efficiency, serie resistance and shunt resistance, respectively. Under simulated AM 1.5 solar illumination at 100 mW/cm^2

A total of five devices was manufactured. The photovoltaic performance of DSSCs based on SnO_2 photoanodes was characterized by current voltage ($J \times V$) measurements under solar simulation. The $J \times V$ curve of the best device is shown in Fig. 8. Photovoltaic parameters are listed in Table 2.

The photovoltaic parameters in DSSCs depends on several factors such as adsorption of the dye by the photoanode material [8, 39] and thickness of the photoanode film [39]. Agglomeration of nanoparticles implies in less active area for dye adsorption, which can result in fewer photoinduced charge carriers with consequent lower short-circuit current. The use of thick films as photoanode can increase series resistance (R_s) values which leads to increased recombination, which can be associated with low fill factor (FF). All these factors together may lead to modest values of power conversion efficiency (η). Despite this shortcoming, the best value of η of 0.53% obtained in this work is similar to values recently reported by other research groups [40].

4 Conclusion

SnO_2 nanoparticles were successfully synthesized using a proteic sol–gel method and applied as photoanode in DSSCs.

Thermal analysis suggested SnO_2 formation at temperatures between 350 and 400 °C. Thermal results showed the presence of residual organic matter not eliminated by the calcination process. A thermal treatment at 600 °C was shown to be efficient to eliminate this residual organic matter. FTIR and UV–Vis results confirmed these findings. XRD results for all samples showed the presence of a single rutile SnO_2 nanostructured phase (crystallite size in the range 8–20 nm with negligible levels of microstrain). TEM results showed nanoparticles with spherical shape and average diameter between 5 and 10 nm.

FTIR, Williamson–Hall, and UV–Vis results showed that the thermally treated samples presented improved crystallinity and superior transparency to visible light. Therefore, these nanoparticles were chosen to be used as photoanodes in the construction of DSSCs that presented photovoltaic parameters consistent with results obtained from similar cells and reported in the literature.

The present work represents an evolution in the production of nanoparticles by an alternative sol–gel process and represents a promising path to applications in emerging technologies.

Acknowledgements The authors are grateful to the Brazilian research agencies Fundação Cearense de Apoio ao Desenvolvimento Cientfico e Tecnológico (FUNCAP) and Conselho Nacional de Desenvolvimento Cientfico e Tecnológico (CNPq) for financial support. Dra. Monica Lira-Cantú and the Catalan Institute of Nanoscience and Nanotechnology (ICN2) for lending infrastructure used to develop this study. SEM measurements were performed at UFC's Central Analtica.

Compliance with ethical standards

Conflict of interest The authors declare that they have no competing interests.

References

1. Chang CH, Gong M, Dey S, Liu F, Castro RHC (2015) Thermodynamic stability of SnO_2 nanoparticles: The role of interface energies and dopants. J Phys Chem C 119:6389–6397
2. Priya SM, Geetha A, Ramamurthi K (2016) Structural, morphological and optical properties of tin oxide nanoparticles synthesized by sol–gel method adding hydrochloric acid. J Sol–Gel Sci Technol 78:365–372
3. Rechberger F, Städler R, Tervoort E, Niederberger M (2016) Strategies to improve the electrical conductivity of nanoparticle-based antimony-doped tin oxide aerogels. J Sol–Gel Sci Technol 80:660–666
4. Beltrán JJ, Sánchez LC, Osorio J, Tirado L, Baggio-Saitovitch EM, Barrero CA (2010) Crystallographic and magnetic properties of Fe-doped SnO_2 nanopowders obtained by a sol–gel method. J Mater Sci 45:5002–5011
5. Diéguez A, Romano-Rodrguez A, Vilà A, Morante JR (2001) The complete Raman spectrum of nanometric SnO_2 particles. J Appl Phys 90:1557
6. Pereira MS, Lima FAS, Ribeiro TS, da Silva MR, Almeida RQ, Barros EB, Vasconcelos IF (2017) Application of Fe-doped SnO_2 nanoparticles in organic solar cells with enhanced stability. Opt Mater 64:548–556
7. Trost S, Becker T, Polywka A, Görrn P, Oszajca MF, Luechinger NA, Rogalla D, Weidner M, Reckers P, Mayer T, Riedl T (2016) Avoiding photoinduced shunts in organic solar cells by the use of tin oxide (SnO_x) as electron extraction material instead of ZnO. Adv Energy Mater 6:1600347
8. Birkel A, Lee YG, Koll D, Van Meerbeek X, Frank S, Choi MJ, Kang YS, Char K, Tremel W (2012) Highly efficient and stable dye-sensitized solar cells based on SnO_2 nanocrystals prepared by microwave-assisted synthesis. Energy Environ Sci 5:5392
9. Pal M, Bera S, Jana S (2015) Sol–gel based simonkolleite nanopetals with SnO_2 nanoparticles in graphite-like amorphous carbon as an efficient and reusable photocatalyst. RSC Adv 5:75062
10. Sun J, Sun P, Zhang D, Xu J, Liang X, Liu F, Lu G (2014) Growth of SnO_2 nanowire arrays by ultrasonic spray pyrolysis and their gas sensing performance. RSC Adv 4:43429
11. Mei L, Chen Y, Ma J (2013) Gas sensing of SnO_2 nanocrystals revisited: developing ultra-sensitive sensors for detecting the H_2S leakage of biogas. Scientific Reports 4:6028
12. Mueller F, Bresser D, Chakravadhanula VSK, Passerini S (2015) Fe-doped SnO_2 nanoparticles as new high capacity anode material for secondary lithium-ion batteries. J Power Sources 299:398–402
13. Ahmed SA (2010) Room-temperature ferromagnetism in pure and Mn doped SnO_2 powders. Solid State Commun 150:2190
14. Ferrari S, Pampillo LG, Saccone FD (2016) Magnetic properties and environment sites in Fe-doped SnO_2 nanoparticles. Mater Chem Phys 177:206–212
15. Shayesteh SF, Nosrati R (2015) The structural and magnetic properties of diluted magnetic semiconductor $Zn_{1-x}Ni_xO$ nanoparticles. J Supercond Nov Magn 28:1821–1826
16. Mehraj S, Ansari MS, Alimuddin (2015) Structural, electrical and magnetic properties of (Fe, Co) co-doped SnO_2 diluted magnetic semiconductor nanostructures. Phys E 65:84–92
17. Inpasalin MS, Choubey RK, Mukherjee S (2016) Evidence of bound magnetic polaron-mediated weak ferromagnetism in co-doped SnO_2 nanocrystals: microstructural, optical, hyperfine, and magnetic investigations. J Electron Mater 45:3562–3569
18. Meneses CT, Flores WH, Garcia F, Sasaki JM (2007) A simple route to the synthesis of high-quality NiO nanoparticles. J Nano Res 9:501–505
19. Nogueira NAS, Utuni VHS, Silva YC, Kiyohara PK, Vasconcelos IF, Miranda MAR, Sasaki JM (2015) X-ray diffraction and Mossbauer studies on superparamagnetic nickel ferrite ($NiFe_2O_4$) obtained by the proteic sol–gel method. Mater Chem Phys 163:402–406
20. Braga TP, Dias DF, de Sousa MF, Soares JM, Sasaki JM (2015) Synthesis of air stable FeCo alloy nanocrystallite by proteic sol–gel method using a rotary oven. J Alloy Compd 622:408–417
21. Santos CM, Martins AFN, Costa BC, Ribeiro TS, Braga TP, Soares JM, Sasaki JM (2016) Synthesis of FeNi alloy nanomaterials by proteic sol–gel method: crystallographic, morphological, and magnetic properties. J Nanomater 2016:1–9
22. Rietveld HM (1967) Line profiles of neutron powder-diffraction peaks for structure refinement. Acta Cryst 22:151
23. Rietveld HM (1969) A profile refinement method for nuclear and magnetic structures. J Appl Cryst 2:65

24. Toby BH (2001) EXPGUI, a graphical user interface for GSAS. J Appl Cryst 34:210
25. Zhao B, Fan B, Xu Y, Shao G, Wang X, Zhao W, Zhang R (2015) Preparation of honeycomb SnO_2 foams and configuration-dependent microwave absorption features. ACS Appl Mater Inter 7:26217–26225
26. Liu J, Li X, Chen X, Niu H, Han X, Zhang T, Lin H, Qu F (2016) Synthesis of SnO_2/In_2O_3 hetero-nanotubes by coaxial-electrospinning method for enhanced formaldehyde response. New J Chem 40:1756
27. Ghodsi FE, Tepehan FZ, Tepehan GG (2011) Derivation of the optical constants of spin coated CeO_2–TiO_2–ZrO_2 thin films prepared by sol–gel route. J Phys Chem Solid 72:761–767
28. Williamson GK, Hall WH (1953) X-ray line broadening from filed aluminum and wolfram. Acta Metall 1:22
29. Aragón FH, Coaquira JAH, Nagamine LCCM, Cohen R, da Silva SW, Morais PC (2015) Thermal-annealing effects on the structural and magnetic properties of 10% Fe-doped Sn_2O nanoparticles synthetized by a polymer precursor method. J Magn Magn Mater 375:74–79
30. Smith BC (2016) The infrared spectroscopy of Alkenes. Spectroscopy 31:28–34
31. Lim AH, Shim HW, Seo SD, Lee GH, Park KS, Kim DW (2012) Biomineralized Sn-based multiphasic nanostructures for li-ion battery electrodes. Nanoscale 4:4694
32. Zhu H, Yang D, Yu G, Zhang H, Kuihong Yao K (2006) A simple hydrothermal route for synthesizing SnO_2 quantum dots. Nanotechnology 17:2386–2389
33. Zhang J, Gao L (2004) Synthesis and characterization of nanocrystalline tin oxide by sol–gel method. J Solid State Chem 177:1425–1430
34. Chen H, Ding L, Sun W, Jiang Q, Hu J, Li J (2015) Synthesis and characterization of Ni-doped SnO_2 microspheres with enhanced visible-light photocatalytic activity. RSC Adv 5:56401
35. Azam A, Ahmed AS, Habib SS, Naqvi AH (2012) Effect of Mn doping on the structural and optical properties of SnO_2 nanoparticles. J Alloy Compd 523:83–87
36. Srinivas K, Vithal M, Sreedhar B, Raja MM, Reddy PV (2009) Structural, optical, and magnetic properties of nanocrystalline Co doped SnO_2 based diluted magnetic semiconductors. J Phys Chem C 113:3543–3552
37. Fang LM, Zu XT, Li ZJ, Zhu S, Liu CM, Zhou WL, Wang LM (2008) Synthesis and characteristics of Fe^{3+}-doped SnO_2 nanoparticles via sol–gel-calcination or sol–gel-hydrothermal route. J Alloy Compd 454:261–267
38. Mandal SK, Nath TK, Das A (2007) Reduction of magnetization in $Zn_{0.9}Fe_{0.1}O$ diluted magnetic semiconducting nanoparticles by doping of Co or Mn ions. J Appl Phys 101:123920
39. Fukai Y, Kondo Y, Mori S, Suzuki E (2007) Highly efficient dye-sensitized SnO_2 solar cells having sufficient electron diffusion length. Electrochem Commun 9:1439–1443
40. Krishnamoorthy T, Tang MZ, Verma A, Nair AS, Pliszka D, Mhaisalkar SG, Ramakrishna S (2012) A facile route to vertically aligned electrospun SnO_2 nanowires on a transparent conducting oxide substrate for dye-sensitized solar cells. J Mater Chem 22:2166